Computers in Biology and Medicine 107 (2019) 97–108

Contents lists available at ScienceDirect

Computers in Biology and Medicine

journal homepage: www.elsevier.com/locate/compbiomed

Realistic forward and inverse model mesh generation for rapid three-dimensional thoracic electrical impedance imaging

Ali Zifan[a], Panos Liatsis[b,*], Hasan Almarzouqi[c]

[a] Department of Medicine, University of California, San Diego, CA, USA
[b] Department of Computer Science, Khalifa University of Science and Technology, Abu Dhabi, United Arab Emirates
[c] Department of Electrical and Computer Engineering, Khalifa University of Science and Technology, Abu Dhabi, United Arab Emirates

ARTICLE INFO

Keywords:
EIT
Thoracic imaging
Mesh generation
Finite elements models
Image reconstruction

ABSTRACT

One of the most promising clinical applications of Electrical Impedance Tomography (EIT) is real-time monitoring of lung function in ambulatory or ICU due to the rapid, non-invasive and non-ionizing nature of the measurements. However, to move this modality into routine clinical use will, as a minimum, require the development of realistic and computationally efficient forward and inverse meshes of the thorax and the lungs alongside mechanisms to extract quantitative information from the resulting reconstructed images. The latter will allow for reduction of artefacts and better localization of conductivity changes within the image domain. This research aims to contribute towards this goal, by introducing a pipeline for the generation of anatomically accurate meshes for EIT forward and inverse models. We achieve this by the segmentation of realistic volumetric data from thoracic CT volumes, and subsequent tessellation. Mesh quality is assessed in terms of aspect ratio, dihedral and face angles. Moreover, the generated meshes are fused with currently available EIT software, with a novel electrode placement method, to show the practical application of the generated meshes. Results show that anatomically constrained unstructured meshes can be generated, conforming to realistic anatomical geometry, and performing well in EIT numerical computations. Such realistic computational models will further enhance the performance of EIT reconstruction algorithms, thus offering significant benefits to clinical EIT lung imaging.

1. Introduction

There is substantial evidence that the electrical properties of tissue vary according to its state of health [1–4], which offers the opportunity to distinguish healthy and abnormal tissue, once these electrical properties are known. Hence, if this latent conductivity distribution among different types of tissue is inferred from measurements, a powerful diagnostic tool could be developed. The problem of conductivity distribution reconstruction from surface measurements is non-linear and ill-conditioned. This can be typically solved using 2D or 3D Finite Element Methods (FEM), subject to appropriate regularization strategies [5,6]. The considerable changes in lung impedance with respiration, and the ease of using impedance tomography as a monitoring technique, led to a significant body of research in lung impedance imaging [7–13]. Current strategies to provide lung protective ventilation rely on avoiding lung overdistension by reducing tidal volumes and on opening atelectasis by applying adequate positive end-expiratory pressure. However, it is currently impossible to continuously measure regional lung overdistension and atelectasis while a patient is ventilated. Indeed, this type of information may produce extremely relevant information that could lead to reducing ventilator-induced lung injuries. Electrical Impedance Tomography (EIT) can resolve changes in the distribution of lung volumes between dependent and non-dependent lung regions as ventilator parameters change. Thus, EIT measurements may be used to control ventilator settings to maintain lung protective ventilation on an individual patient basis [11,14–16].

In spite of the aforementioned advantages, EIT still suffers from certain limitations that could impede its adoption in routine medical diagnosis. It is well known in theory that a reconstructed EIT image is unique for noise-free, complete boundary data [16]. However, in practice, EIT suffers from poor spatial resolution due to noise, low sensitivity of boundary voltages to inner conductivity perturbations and the limited number of boundary voltage measurements [17]. Moreover, reconstructed images are usually difference (rather than static) images due to the application of the linearization process, which prevents the use of EIT in diagnosis of a number of diseases and makes it less comparable to other medical imaging modalities, such as CT and MRI. An additional challenge is that EIT patient histories generally include

* Corresponding author.
E-mail address: panos.liatsis@ku.ac.ae (P. Liatsis).

https://doi.org/10.1016/j.compbiomed.2019.02.007
Received 29 August 2018; Received in revised form 13 February 2019; Accepted 13 February 2019

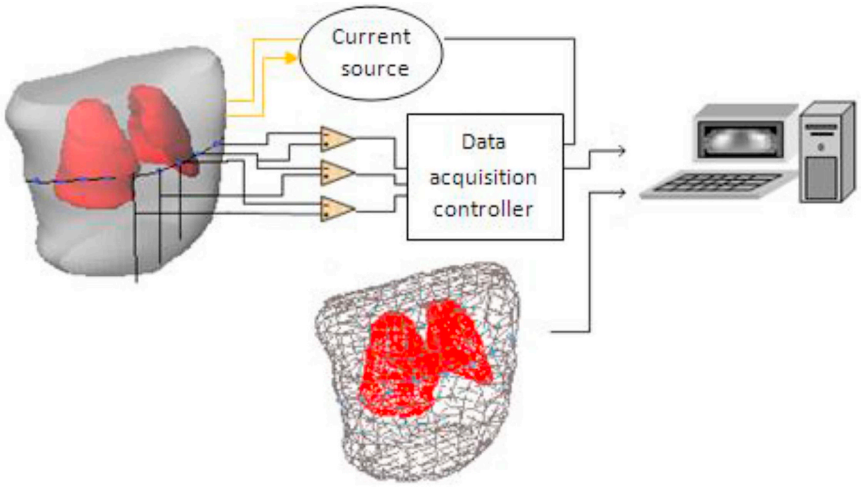

Fig. 1. EIT imaging system: Rotating current injection (I) is performed between pairs of adjacent surface electrodes (shown in blue color) on a cross-section of the human thorax, and resulting voltages (V) are measured between other pairs of electrodes and passed to a PC for impedance distribution reconstruction.

data from a limited battery of tests, thus, making it difficult to train sufficiently complete models to study the functional behavior of various human organs.

An attempt was made to develop a consensus in one aspect, i.e., a linear reconstruction algorithm for lung EIT, known as GREIT (Graz consensus Reconstruction algorithm for EIT) [18]. However, latter work focused on applying the GREIT algorithm on a 2D grid, which neither incorporates the lungs in the 3D forward model, nor uses any standards for EIT lung image interpretation. A number of contributions were made to support 3D imaging in real time, optimal electrode placement, and measuring the associated image quality [19–23].

Considering the existing progress and challenges, and focusing on developing dynamic yet realistic FEM models, it is appropriate to build shape models, which not only incorporate realistic human thorax and lung information but also exhibit comparable functional behavior. The latter aspect requires the development of a framework for such ready-to-use FEM models. Although there exists a spatial resolution limit that can be achieved independently of mesh density, the use of very coarse meshes will result to model geometries, which are far from realistic, thus biasing the final solution. Realistic patient-specific EIT computational models need to provide a realistic Finite Elements model and subsequently, a basis for generating new datasets. Moreover, such models could serve as a platform for creating statistical shape priors and used for the regularization of the inverse problem.

Modelling sensitivity distributions for various measurement schemes requires solving a number of computational problems using high-resolution anatomically accurate 3D models. The main advantages of structured meshes are their simplicity and the fact that they lend themselves to high order difference operators. Their main disadvantage is that they are more difficult to apply in geometries with multiple connectivity and/or to problems with irregular boundaries (e.g., lobes). Moreover, structured meshes are also not well suited for local mesh refinement; that is, refinement of the mesh local to a particular region of space, without affecting the mesh resolution away from that region [24].

Since the human body represents a complex non-homogeneous and non-isotropic medium with a variable cross-section area, the fundamental issues are the nature and relative contribution of various organs and tissues to the bioimpedance signal. Thus, modelling sensitivity distributions for various measurement schemes requires solving a number of computational problems using high-resolution anatomically accurate 3D models. Unstructured meshes are naturally adapted to represent domains of arbitrary connectivity, or with boundaries of arbitrary shapes. They can also be refined locally.

Considering the above, in this work, we tackle one very important and quintessential aspect of the problem, specifically, the generation of anatomically-valid, unstructured thoracic meshes for both the forward and inverse models. In summary, the novelties introduced by the current work include: (i) Rapid 3D image reconstructions, using realistic 3D forward and 3D inverse thorax meshes, and (ii) A new framework for the generation and attachment of electrodes onto arbitrary 3D meshes in the context of 3D EIT imaging.

2. Background

2.1. Image reconstruction in EIT

In EIT, typically a current (≈ 1 mA) is injected through a single (or multiple) ring of electrodes, attached around the medium under study. Current is injected into one electrode pair and the voltages between other electrodes are then recorded. When using the adjacent protocol, current injection is successively shifted so that all electrode pairs are used based on a single frequency (typically 50 kHz) or multiple frequencies (up to 1 MHz). The governing equation for the voltage field produced across the body Ω is [25]:

$$\nabla(\sigma + \omega\varepsilon)\nabla\phi = 0 \tag{1}$$

where σ is the electric conductivity of the medium, ϕ is the electric potential, ω is the frequency, and ε is the electric permittivity. In order to estimate σ, two interconnected problems, i.e., forward and inverse, need to be solved. The forward problem relates to determining the voltage distribution for a known conductivity distribution in the imaged domain, while the inverse problem consists of conductivity image reconstruction using the measured voltages at the surface of the medium. Fig. 1 shows a high level overview of this process for the adjacent current injection protocol, where actual measurements taken from the body (shown in solid grey) are combined with the voltages obtained from a mathematical model (shown in grid form) in order to obtain the reconstructed conductivity image.We represent the forward operator g by $g(m) = d$, where m is the model and d is the boundary measurement voltage vector. The goal is to come up with the model, which yielded the actual measured voltages, denoted by d_T. The simplest approach to achieve this is by minimizing the sum of squared errors [25]:

$$|| d_T - g(m) ||_F^2 \tag{2}$$

where F denotes the Frobenius norm.

We assume no model null-space and that only the data misfit term as described in Equation (2) is required to solve the inverse problem. Thus,

by linearizing the g operator, we may employ linear methods, e.g., Conjugate Gradient (CG), to derive the critical points of Equation (2). This is achieved by linearizing the forward problem in the neighborhood of the reference model m_0, using Taylor series expansion:

$$g(m) = g(m_0) + \left.\frac{\partial g}{\partial m}\right|_{m=m_0}(m - m_0) + \left.\frac{\partial^2 g}{\partial m^2}\right|_{m=m_0}(m - m_0)^2 + \ldots \approx g(m_0) + \nabla g(m_0)(m - m_0) + \ldots \quad (3)$$

Ignoring the higher order terms,

$$g(m) = g(m_0) + G(m - m_0) \quad (4)$$

where G is a rectangular matrix that gives the sensitivity of the forward problem to the model parameters at $m = m_0$:

$$G_{ij} = \left.\frac{\partial g_j}{\partial m_i}\right|_{m=m_0} \quad (5)$$

Next, we use Taylor series expansion to linearize the inverse problem:

$$d = g(m) \approx g(m_0) + G(m - m_0) \quad (6)$$

Let $\delta d = d - g(m_0) and\ \delta m = m - m_0$ denote the perturbations, so

$$\delta d = G\delta m \quad (7)$$

which is the linearized inverse problem for the perturbation of m about. $m = m_0$.

As the problem is ill-posed, i.e., small errors in the measurements may introduce large errors in the reconstruction, the minimization of the voltage error in Equation (2) is not likely to yield sufficiently good results. This is because, in practice, linear Least Squares calculations usually involve singular matrices or matrices that are close to being numerically singular, i.e., small eigenvalues. For a unique solution, additional information about the conductivity is required, which is known as the prior. Regularization mitigates these singularities. This can be done by discarding small eigenvalues or penalizing the magnitude of acceptable solutions and the data misfit. In other words, the minimization problem of Equation (2) can be written as [25]:

$$\min\left(\| \delta d_T - G(\delta m) \|^2 + \lambda \| R\delta m \|^2\right) \quad (8)$$

The first part of Equation (8) is the data misfit, while the second part is the regularization term. The fudge factor (or hyperparameter) λ controls the trade-off between the two terms and not only considers the possibility of minimizing the norm of δm, but also the norm of some linear function (i.e., R) of the mode. When $R \equiv \partial^n$, $n = 0,1,2, \ldots$ and ∂^n is an n-th order discrete difference operator, the second term in Equation (8) penalizes the slope, roughness, or higher order derivatives of the model, respectively.

3. Methodology

3.1. System overview and image pre-processing

The proposed pipeline for realistic 3D forward and inverse mesh generation entails a framework for the segmentation of CT volumes of the thorax to the actual tetrahedral mesh generation and attachment of electrode rings, as shown in Fig. 2. To further evaluate the meshes, following electrode attachment and tetrahedralization, the EIT elliptical differential equation is solved on the volume meshes using fast 3D-3D, forward-inverse, dual models in order to produce conductivity images of the thorax.

In order to segment the CT images, as there are many stacks of slices, the goal is to use techniques that require little or no manual intervention. For each CT volume, we start by thresholding slices using the algorithm proposed in Ref. [26]. This iterative method computes the value of a threshold so that two groups of pixels, i.e., foreground and background, are well separated. It works as follows: Let T_i be the threshold value at step i and μ_1, μ_2 be the average intensities of the body pixels and non-body pixels, respectively. Then, the threshold for step $i + 1$ is set to the mean of μ_1, μ_2. The threshold updating procedure is repeated until there is no change in the threshold value, i.e., $T_{i+1} = T_i$. A sample thresholded image of one of the training images is shown in Fig. 3(b).

To extract the thoracic wall, the image is inverted, holes are filled using region filling and the resulting image is labelled as thorax and assigned a value of '1', as shown in Fig. 3(c). The lung lobes are segmented by removing the background in Fig. 3(b). Here, background pixels are identified as follows: they are non–body pixels and connected to the borders of the image. Thus, every connected region of non–body pixels, which touches the border is considered as background and discarded. Next, the lung lobes are filled, which results to the image of Fig. 3(d). In order to extract the bone structures, as the intensity of the bones is much higher than that of the surrounding tissues, we threshold the CT image using the 0.96 quantile, fill in the holes of the resulting images and remove any remaining isolated pixels. This results in the image of Fig. 3(e). Finally, by assigning different labels, we obtain the multi-labelled image in Fig. 3(f). A complete segmentation of the volume set is shown in panels (g-i) of Fig. 3.

3.2. Dataset

For the experiments, we used the sequences from the POPI-model [27], obtained from the Léon-Bérard Cancer & CREATIS Lab Center, France. The images were acquired using a Philips 16 Slice Brilliance CT Big Bore Oncology™ configuration. Each slice of the DICOM files has a resolution of 0.976562 mm × 0.976562 mm × 2 mm. The size of the 3D volume is 512 × 512 × 141 voxels. As the objective is to create Finite Element models for simulations that may require matrix inversion, it was necessary to reduce the dimensions of the input dataset. The images were cut in the X and Y dimensions to the smallest size still containing all patient features. The images were then reduced by retaining every third point in the X and Y dimensions to get a final working image of 161 × 121 × 141 voxels.

3.3. Electrode generation and placement

The structure and performance of the electrode system greatly influences the original information extraction, real-time properties of the system, image resolving power, and in particular, information

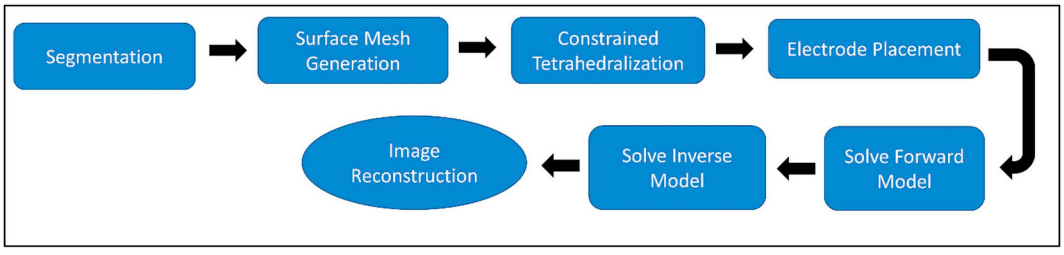

Fig. 2. Thoracic imaging system overview.

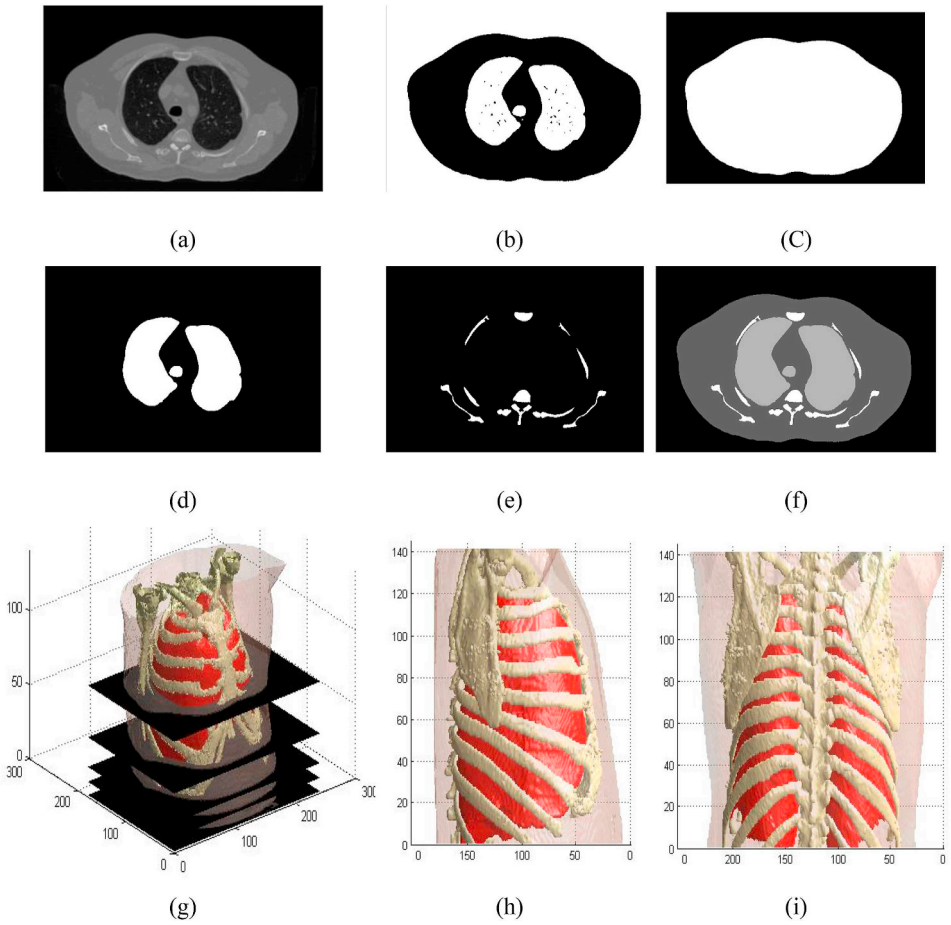

Fig. 3. Segmenting a CT slice: (a) Cross-section of chest CT, (b) Thresholded image, (c) Thorax region, (d) Lung lobes and trachea, (e) Bone structures, (f) Multi-labelled segmented image, (g) 3D reconstruction, (h) Lateral view, (i) Ventral view.

extraction from the center area, where EIT measurement sensitivity is poor, making the design of the electrode system, a pivotal part of any EIT system. Because the imaging area of EIT is often circular or spheroidal, some important structural parameters of the EIT electrode, such as the electrode width, the distance between electrodes, etc, impose restrictions on each other. The mutual influence of these parameters is rather complex, which makes the design and parameter selection of the electrode configuration an arduous task. In practice, electrodes can be made of larger or smaller areas resulting in smaller or larger inter-electrode gaps, respectively, representing a trade-off, i.e., larger electrodes provide better contact, however the resulting inter-electrode gap is smaller, thus leading to larger shunting currents from the electrodes, which are not involved in excitation. This shunting ultimately reduces the ability of the probe to sense at distance, as a fraction of the injected current does not travel into the tissue, but rather has a return path through the electrode array itself.

Electrode generation on an unstructured mesh constitutes a major challenge as incorrect modelling of electrode dimensions may affect the FEM simulations, since they are the lead fields for current injection and pick-up. In order to create good quality electrodes, the thorax mesh needs to be locally refined in order to accommodate for the electrodes. Electrodes placed at a mid-thoracic level show a good approximation of the global lung behavior [28]. Placing electrodes too low may result in a large contribution of mediastinum or abdominal impedance changes in the center of the EIT image.

In what follows, we describe the development of an automatic method for placing 16 circularly shaped electrodes on an unstructured mesh. Any number of electrodes can be used as long as the restrictions of inter-electrode spacing are adhered. The proposed algorithm only requires the definition of the Z coordinate at which the electrodes need to be placed. The algorithm works as follows: Once the Z coordinate is specified, e.g., at z_l, the thoracic mesh is cut through with a plane perpendicular to the Z-axis at z_l. Next, in order to find the intersection points, the coordinates, where the edges of each mesh element, in the neighborhood of z_l, intersect the plane are calculated. This is performed using the concept of the intersection of a plane with a triangle. Using the plane equation in vector form, $n\cdot(X - X_0) = 0$, where n is a unit-length normal vector, X a point position vector, and X_0 a point position vector at some point p_0, a point p_k is situated on the left side of the plane, when $n\cdot(p_k - X_0) > 0$, on the right side of the plane, when $n\cdot(p_k - X_0) < 0$, and finally, on the plane itself, when $n\cdot(p_k - X_0) = 0$.

The problem of finding the intersection of mesh elements with a plane can be simplified, by considering a triangular element as a combination of three edges (or lines). Thus, the problem of finding intersections can be reduced to that of finding the intersection of lines and a cutting plane. However, in order to find such intersecting edges, the location of each edge node needs to be determined. We are only interested in edges whose nodes lie on both sides (upper and lower) of the cutting plane. These edges can be found using the aforementioned formulation of the signed distance function of a point from a plane.

We determine these edges by going through each element and applying the distance rule, and only preserve the element edges whose nodes are situated at opposite sides of the plane. Once the edges are selected, their intersection points with the cutting plane are determined using the shape shown in Fig. 4. As shown in the figure, for a point M to be on the plane, Equation $n\cdot(M - X_0) = n\cdot M - w = 0$ must hold, where w is a scalar. Moreover, for point M to be located on the line connecting edge points $p_1(x_1, y_1, z_1)$ and $p_2(x_2, y_2, z_2)$, it should satisfy the line

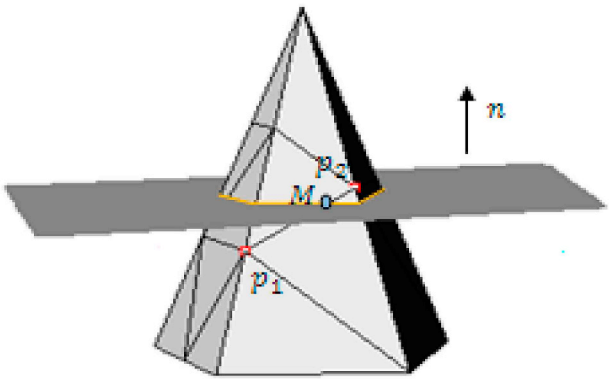

Fig. 4. Mesh elements clipped by a plane.

equation, $M = p_1 + (p_2 - p_1)t$, $t \in [0,1]$. Substituting this into the plane equation and solving for t, we obtain

$$t = \frac{n.\ p_1}{n\cdot(p_1 - p_2)} = \frac{w_1}{w_1 - w_2} \tag{9}$$

where $w_k = n.\ p_k$ for $k = 1, 2$. Therefore, the point of intersection is given by,

$$M = p_1 + \frac{w_1}{w_1 - w_2}(p_1 - p_2) \tag{10}$$

This process is performed for all selected edges, thus resulting to the set of mesh intersection coordinates. However, these coordinates cannot be used as electrode centers as they do not necessary adhere to the equal inter-electrode spacing requirement. In order to resolve this, the cloud of mesh intersection points is approximated using MATLAB's spline interpolation function with 16 control knots, i.e., the number of control knots is set equal to the number of electrodes. The end product of this process is a set of equally spaced points around the thorax at the defined height/slice. Once these coordinates are determined, the corresponding elements that the points fall into on the thorax mesh are marked and passed on to the refinement step.

The marked elements and their neighbors are the input to the local refinement step. In order to refine the mesh locally, we use the Red-Green-Blue (RGB) subdivision method [29]. This generates the same limit surface of the Loop subdivision [30], independently of the order of application of local operators. It also supports dynamic selective refinement and generates conforming meshes at all intermediate steps.

3.4. Tetrahedral mesh generation

The problem of generating high quality FEM meshes of the human body remains a significant barrier to progress in EIT. The mesh must be sufficiently fine to represent potentials with the necessary accuracy to predict the measured voltages as a function of conductivity. In turn, this sets the requirements for the accuracy of representation of the surface shape of the region to be meshed, and the geometry of the associated electrodes. The mesh needs to be finer in areas of high field strength, and in particular, near the edges of the electrodes. TetGen was used for tetrahedral mesh generation [31]. TetGen offers a suite of techniques to generate tetrahedral meshes from three-dimensional point sets or domains with piecewise linear boundaries. In particular, we employed the module that computes the Constrained Delaunay Tetrahedralization (CDT) from the isosurface mesh produced by the Computational Geometry Algorithms Library (CGAL).

During tetrahedralization, bone structures are not used as this requires a finer mesh in these regions, which would heavily impact on the total number of elements and associated computations. Moreover, as difference imaging is used, bone structures will not be visible in the final EIT image since the associated conductivity changes are considered negligible, however, this assumption is not always true [32]. Instead, the thoracic wall and lung surface meshes are used in the tetrahedralization process. TetGen assumes that the surfaces of the input objects are already meshed and represented as a polyhedron. This polyhedron is also known as a Piecewise Linear Complex (PLC). The output is a constrained Delaunay volume mesh that contains quality tetrahedral elements. The implementation first generates a new surface mesh and then a tetrahedral mesh using a size parameter to control the resolution, which was set to 2. This setting was used at the surface mesh generation stage for both the lobes and the thoracic wall. Larger size numbers did not yield any tetrahedralization, as this would result in intersecting facets in the tetrahedralization step.

There are several quality measures in the literature for tetrahedral volume meshes. In this research, we used the quality measures available in TetGen. For high accuracy FE meshes, it is generally necessary that the shapes of tetrahedra have bounded aspect ratios. The aspect ratio of a tetrahedron is the ratio of the maximum side length to the minimum height. For a quality mesh, this value should be as small as possible. A similar but weaker quality measure is the radius-edge ratio. The radius-edge ratio Q is the ratio of the circumsphere radius R to the length of the shortest edge L, defined as $Q = R/L$. For all well-shaped tetrahedra, this value is small, while for most badly-shaped tetrahedra, this value is large. After tetrahedralization, automatic mesh quality evaluation is performed and a mesh quality report on the smallest and largest volumes, the shortest and longest edges, the smallest and largest dihedral angles, radius-edge ratio histogram, aspect ratio histogram, dihedral angle histogram is generated by TetGen.

3.5. Sensitivity field

The sensitivity of the voltage measurements to variations in the conductivity distribution can be computed with the forward model. Initially, the lead field is often unknown, but may be found by FEM modelling to the extent that the volume dimensions and conductivity distribution are known. The lead field illustrates the sensitivity distribution of the pick-up electrodes (PU) for current carrying (CC) electrodes. For tetrapolar measurements, the change in the voltage difference, $V_m - V_n$, or sensitivity to a variation in the conductivity distribution, $\delta\sigma$, given that the current was injected through the electrode pair (i, j) is given by Ref. [25]:

$$\delta(V_m - V_n) = -\int_{\Omega} \delta\sigma E_{PU(m,n)}\cdot E_{CC(i,j)} \tag{11}$$

where $E_{CC(i,j)}$ is the actual electric field resulting from the applied current at electrode pair (i,j), and $E_{PU(m,n)}$ is the electric field that would result from the application of a unitary current stimulus at measurement pair (m, n). Moreover, optimum electrode configuration is crucial in order to focus the measurements on the desired tissue volume.

The sensitivity of a transfer impedance measurement in a limited volume with four surface electrodes can be determined by examining the dot product, as in Equation 11 (also see Fig. 5). In some volume positions where the vectors are perpendicular to each other, the measured impedance is insensitive to local resistivity changes. In other positions, the angle is $> 90^{\circ}$, thus, sensitivity is reversed.

3.6. Image reconstruction

In order to perform image reconstruction, EIDORS was used [33,34]. EIDORS is an open source software suite for image reconstruction in EIT and diffuse optical tomography. We assume that the smoothness of the conductivity distribution is isotropic within the thorax and lungs. As the number of elements is high, a dual reconstruction model is employed in the simulation studies. The dual reconstruction model uses a fine FEM mesh to implement the forward solution, and a coarser FEM mesh for the inverse solution. The $2^{1/2}$ -D assumption from the Geophysics community [35] is invoked that all

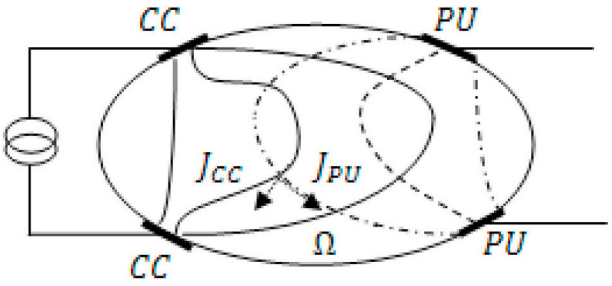

Fig. 5. Four-electrode system with current density and reciprocal current density lines. Sensitivity is shown at a single point. The dot product of the two current density vectors and therefore, the sensitivity is small, as the vectors are nearly perpendicular.

source and receiver electrodes are co-planar at $Z = 0$. In other words, the medium properties are assumed to be constant in the Z direction.

3.6.1. 3D-3D dual reconstruction

The quality of the generated meshes was tested on FEM simulations for the solution of the forward and inverse problems using EIDORS [34]. As a 3D inverse model is used, it is of paramount importance to correctly model the 3D flow of current inside the thoracic volume. This was achieved by increasing the number of electrode rings to two in order to increase the resolution of the simulations in the Z direction. The resulting simulations were fast, compared to those on finer meshes.

In the employed 3D-3D method, the forward problem was solved on the fine mesh, using a forward operator F, which takes the initially assigned element conductivity values, σ_{fine}, and produces the voltages at each node of the mesh, i.e., $V = F(\sigma_{fine})$. Next, the reconstruction model was defined over the coarse mesh, where the element conductivities on this mesh, σ_{coarse}, are related to the conductivity values of the fine mesh by a matrix multiplication, i.e., $\sigma_{fine} = P\sigma_{coarse}$. Each element $[P]_{i,j}$ represents the fraction of the fine element i enclosed in the coarse element j. Next, the Jacobian matrix was defined over the coarse J_{coarse} and fine J_{fine} meshes as follows:

$$v = J_{fine}\sigma_{fine} = J_{fine}P\sigma_{coarse} = J_{coarse}\sigma_{coarse} \quad (12)$$

where $J_{coarse} = J_{fine}P$. As the Jacobian matrix of the fine mesh is quite large, EIDORS uses an adjoint approach to calculate it.

4. Results

All reconstructions were carried out using MATLAB 2010a (Mathworks Inc.) using an Intel Xeon 5130, 2.00 GHZ processor with 3.25 GB of RAM.

4.1. Electrode placement

We performed RGB refinement on the thorax mesh in order to refine it near the electrodes. Once the mesh is locally refined, the faces within a specified radius of the center were found. An example result of this process is shown in Fig. 6. In this particular setting, the mesh was cut along the Z coordinate at the 70th slice. The coordinates of the intersections and their respective centers were extracted using B-splines and refined using the RGB algorithm.

In general, due to the unstructured nature of the mesh, the generated electrode surfaces do not occupy the same area. This is an undesirable outcome as it affects the contact surface area of the electrode. This would lead to a variation in the amount of injected current per unit area at different electrode positions. Thus, it was necessary to ensure that all electrodes have equal surface areas. To achieve this, the electrode with the minimum number of faces among the set of 16 electrodes was determined and the surface areas of the remaining 15 electrodes were modified, by iteratively removing the faces furthest from the center. This process was performed until all electrode surface areas become equal or the surface area variance meets a pre-specified threshold criterion. In the mesh of Fig. 6, a variance of 0.012 between electrode surface areas was achieved.

4.2. Tetrahedral mesh generation

The result of the tetrahedralization process and associated mesh statistics for the volume of Fig. 6 with incorporated lungs are shown in Fig. 7 and Table 1, respectively. For all meshes used in the simulations, the radius-edge ratio of the tetrahedron was set to 1.4 to ensure a good quality mesh. The fine mesh of Fig. 7 is comprised of 48052, 257660, 528814 points, tetrahedra and triangles, respectively. The number of elements in the final mesh could be further reduced if regions of high field strength inside the object and where the potential gently decreases are found.

Considering the parameters of Table 1, starting from the aspect ratio parameter, which is a measure of the quality of an element (i.e., ratio of the diameter of the enclosing sphere to the diameter of the enclosed sphere), an ideal aspect ratio is close to unity. It can be observed that the aspect ratio of 693 elements is greater than 10, which is on the high side (five being a good upper bound goal).

However, 92.21% of the elements fall below the aspect ratio value of 5, which is acceptable [36]. Next, we inspect the dihedral angles parameter in the table. This parameter ultimately determines the success of any FEM, i.e., large dihedral angles cause large interpolation and discretization errors, robbing subsequent numerical simulations of their accuracy, while small dihedral angles render the stiffness matrices associated with the FEM method fatally ill-conditioned [37]. In general, dihedral angles of a well-sized tetrahedral mesh are bounded between 10.7° and 164.8° [37]. According to Table 1, 99.73% of the generated dihedral angles fall between the recommended values, which confirms the good quality of the generated mesh. Finally, the values of the face angles reveal that 99.99% of face angles lie above 10°, which reinforces that mesh quality is accurate and acceptable.

4.3. Image reconstruction

- 3D-2D reconstruction

EIT simulations using 3D meshes for both the forward and inverse problems based on a realistic model of the thorax including the lungs were performed. For the initial 3D forward, 2D inverse reconstruction, simulated data were generated using two 3D FEM meshes with 45998 and 257660 elements (i.e., mesh of Fig. 7), respectively. The former uses a circular inclusion, while the latter is adapted to the lungs with a larger number of elements, based on the complete electrode model and trigonometric current patterns [38]. Data for the reference frame was generated using a homogenous background conductivity with $\sigma_0 = 1$. The inverse problem was solved using the regularization procedures previously described using a $2^{1/2}$ -D reconstruction.

4.3.1. Sensitivity distribution

The sensitivity field between electrode pairs (6, 7) and (14, 15) is shown in Fig. 8 for the mesh of Fig. 7(a). It can be seen that sensitivity remains high near the electrode regions, where current was injected. The reciprocal current density J_{PU} near the electrodes is very high, and one may be led to believe that sensitivity is high in this zone.

The pick-up electrode pair should be appropriately positioned so that the corresponding volume is in a high sensitivity zone of the PU electrodes in order to detect interesting physiological processes taking place in the tissue. Fig. 8 demonstrates that the dot product $J_{PU} \cdot J_{CC}$ has high values near the PU electrodes.

4.3.2. 3D thoracic current density distribution

To visualize the current density distribution in 3D, a 0.3 change in

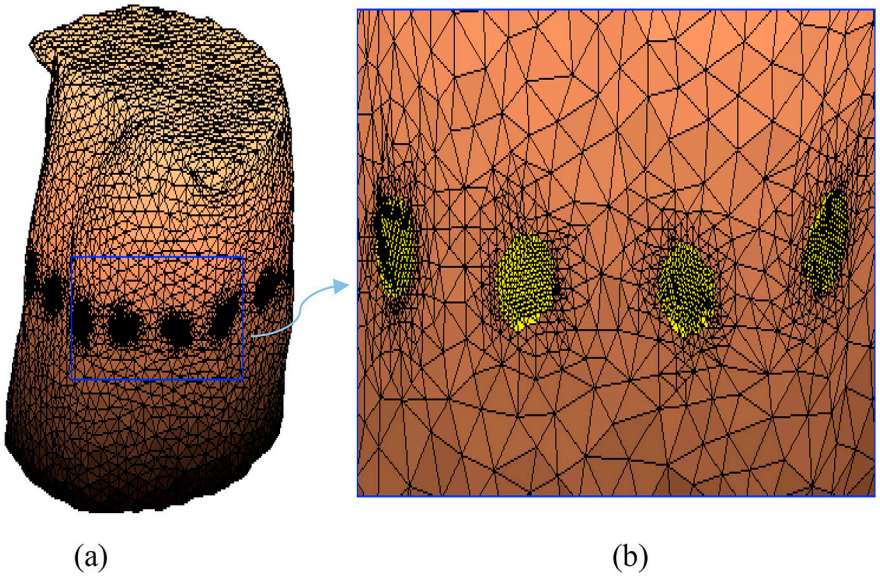

Fig. 6. Electrode generation: (a) Selected elements are adaptively refined using the RGB algorithm and finally a radius is selected to enclose all faces lying underneath a particular electrode to comprise the final electrode, (b) zoom-in version.

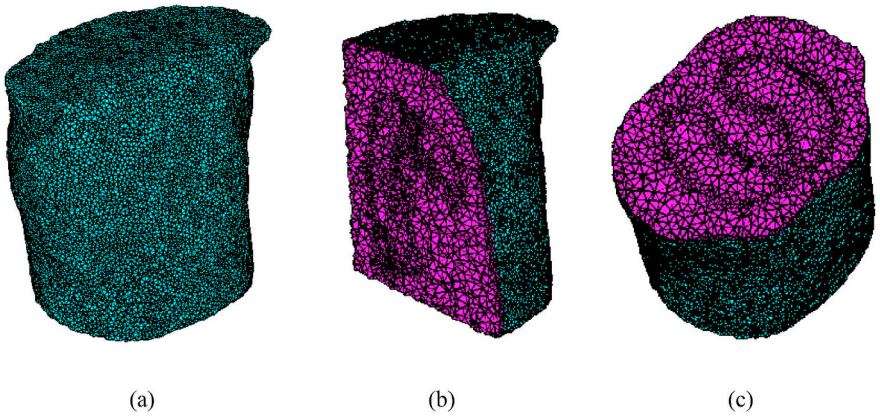

Fig. 7. Tetrahedralization of the thorax and the lobes: (a) Surface view, (b) Side view, (c) Cross-sectional view.

Table 1
Mesh statistics.

Aspect ratio histogram		Histogram (degrees)	Dihedral angle	Face angle
< 1.5:	4628	0-10:	1393	23
1.5–2:	56236	10-30:	46659	61964
2–2.5:	77174	30-50:	146662	359375
2.5–3:	55265	50-70:	62946	213393
3-4:	42896	70-80:	4058	176509
4-6:	15049	80-110:	159308	232386
6-10:	5719	110-130:	61951	13803
10-15:	661	130-150:	23980	172
15-25:	28	150-160:	6274	2
25-50:	4	160-170:	2089	1
50-100:	0	170-175:	0	0
100-:	0	175-180:	0	0

conductivity was applied to the lung regions in order to simulate the effect of an inhomogeneity. Here, the mesh is adapted to the lung lobes, which results in the ultra-fine mesh of Fig. 7 and re-displayed in Fig. 9(a) with the electrodes attached. In this mesh, as the resolution of the volume mesh is high, there is no need for refinement near the electrode regions. This was done following the use of the same forward solver to generate simulated data with no noise to evaluate whether the simulated conductivities can be recovered well using a variety of a priori assumptions. The simulated data used 16 equi-spaced electrodes on a plane driven with the adjacent current drive protocol. Fig. 9(b) shows the use of the L-curve method for the choice of the hyperparameter. This method plots the semi-norm of the regularized solution, $\log_{10} \| M\hat{\sigma} \|$ versus the norm of the corresponding residual vector, $\log_{10} \| J\hat{\sigma} - V_1 \|$, parametrically over λ. The most suitable value of the regularizing parameter λ is determined by selecting one intermediate point on the corner of the L-curve. Measurements involving one or more of the driving electrodes were discarded giving 208 independent measurements per data frame. The estimated current density is shown as a vector field in Fig. 9(c and d). This figure demonstrates the non-planar nature of current streamlines and why it is not possible to apply CT reconstruction algorithms for use in EIT, as current cannot be confined to flow on a 2D plane. The change in direction of the current streamlines as current passes through regions of varying conductivity can also be observed.

For the aforementioned mesh, the resulting reconstructions did not generate clear delineations of the lobes, as shown in Fig. 10. This underlines the lack of suitability of using 3D-2D dual models for lung EIT, particularly, in the context of the axial variability of the lungs in the thorax. In summary, the ultrafine mesh of Fig. 7, supported by the statistics of Table 1, provides an accurate platform for solving the forward problem, and generating synthetic data. However, as its large dual reconstruction models use a high density FEM to implement the

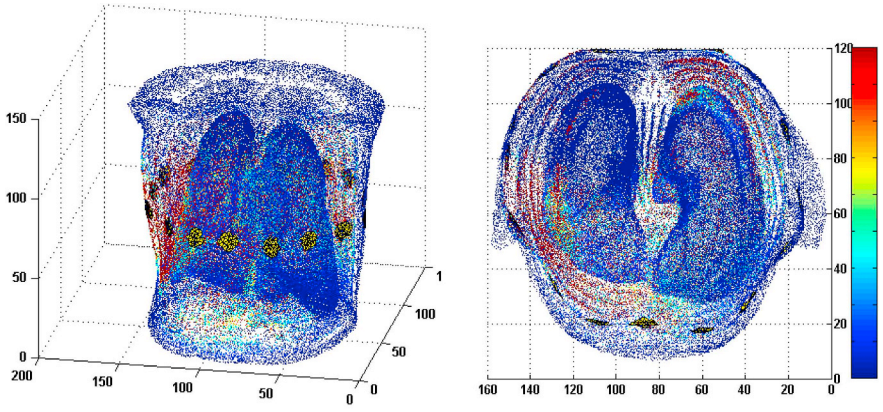

(a) (b)

Fig. 8. Sensitivity is illustrated at tetrahedral centroids: (a) frontal view, (b) top view. Red and blue regions refer to regions of maximum and minimum sensitivity, respectively.

forward solution (voltages at electrodes), and a low density mesh for the inverse solution, the 3D-2D approach was not able to produce sufficiently good reconstructions.

- 3D-3D dual reconstruction

The challenge in achieving faster simulations is to maintain the realism of the topology of the mesh in Fig. 7, while significantly decreasing the number of tetrahedral elements. The latter objective can be achieved if the mesh does not contain interior organs, thus allowing the use of mesh decimation techniques to reduce the size of the interior elements [39]. In this research, the size of the mesh was reduced, by first, sampling every second point in the *X*, *Y* and *Z* directions. Moreover, TetGen offers an option, the *'-pq'* switch, which creates volumes, containing other sub-volumes, where the size of the meshes is well-graded with respect to the input boundary [40], i.e., in the thoracic wall, mesh size is small near the boundary and gradually increases in the interior. The statistics of the forward mesh are shown in Table 2, under the entry for forward (FWD) mesh. A 3D mesh, which does not contain the lungs, is employed in the inverse stage, thus simplifying the meshing process and keeping the number of tetrahedral elements relatively low. The statistics of the inverse (INV) mesh are shown in Table 2. It is important to emphasize that it is not possible to use the same model mesh for the solution of both the forward and inverse problems, as this would constitute an inverse crime.

The inverse mesh of Table 2 is comprised of 6972 tetrahedra and 1432 vertices. By examining the entries of Table 2, only 5 elements have aspect ratios greater than ten, while the remaining elements fall within acceptable margins [37,40]. Next, by inspecting the dihedral angles of the table, and considering that dihedral angles of a well-sized tetrahedral mesh are bounded between 10.7° and 164.8°, it can be observed that 99.89% of all dihedral angles fall within acceptable values. Finally, the values of the face angles reveal that they all lie above 10°, which is another indication of the quality of the generated mesh. According to Table 2, the forward tetrahedral mesh is comprised of 46219 tetrahedra and 9139 vertices, respectively. Going through the entries of the table, only 300 elements have aspect ratios greater than ten, while the remaining elements fall within acceptable margins. More than 89.9% of the dihedral angles fall between 10.7° and 164.8°, which is an indication of the good quality of the mesh. Finally, almost 99.9% of the values of the face angles are above 10°.

The inverse mesh of Table 2 is comprised of 6972 tetrahedra, which is considerably smaller than the mesh of Fig. 7, consisting of 257660 tetrahedra. To test the performance of the generated meshes, FEM simulations for the solution of the forward and inverse problems were carried out in EIDORS. As the 3D inverse model is used, it is of paramount importance to correctly model 3D current flow inside the thorax. This was achieved by using two electrode rings to increase the resolution in the *Z* direction. The resulting simulations were fast, when compared to those with the finer meshes. It takes on average 1.14s and 0.53s to solve the forward and inverse problems, respectively. These are significant improvements in EIT 3D reconstruction, when considering the 3D nature of the inverse model. In the employed 3D-3D method, the forward problem was solved on the fine mesh. The reconstruction model was defined over the coarse mesh. As the Jacobian matrix of the fine mesh is quite large, EIDORS uses an adjoint approach to calculate this.

Using the spatial extent of the lungs as ground truth, it was possible to estimate the accuracy of the reconstructions, when it comes to recovering the volume of the lung lobes in their entirety. In order to carry out the former, the volume sum of each element corresponding to the left and right lobes in the original mesh was calculated and the same process of volume calculation was performed in the segmented volume mesh of Fig. 11(c).

As an unstructured mesh was used, the volume of each tetrahedron varies. The original volume of Fig. 11(a) was calculated in terms of the number of voxels to be equal to 4.5747e+004, while the thresholded conductivity mesh of Fig. 11(c) gives a total of 3.0806e+004 voxels. Therefore, the reconstruction makes up to 67.34% of the original volume. Reconstruction accuracy can be further improved by increasing the value of the hyperparameter, however, to the expense of introducing artefacts outside the locations of the lobes. This may be problematic in instances where the original shape of the lungs is unknown. Naturally, increasing the number of electrode rings will also contribute in improving the quality of the reconstructions by increasing the resolution along the *Z* direction.

5. Discussion

A system pipeline for generation of quality meshes in EIT forward modelling and inverse reconstruction simulations was introduced. Additional investigations into the behavior of the generated meshes under different current patterns, multiple electrode rings, types of reconstruction algorithms and associated priors are not within the scope of the current work. When designing EIT solutions, there are two fundamental aspects, which need to be carefully considered. First, the use of additional electrodes will not result in significant gains in resolution near the center of the mesh. Second, care should be placed in avoiding the use of meshes, which are significantly finer than the smallest variations in conductivity that the EIT system can distinguish as this will

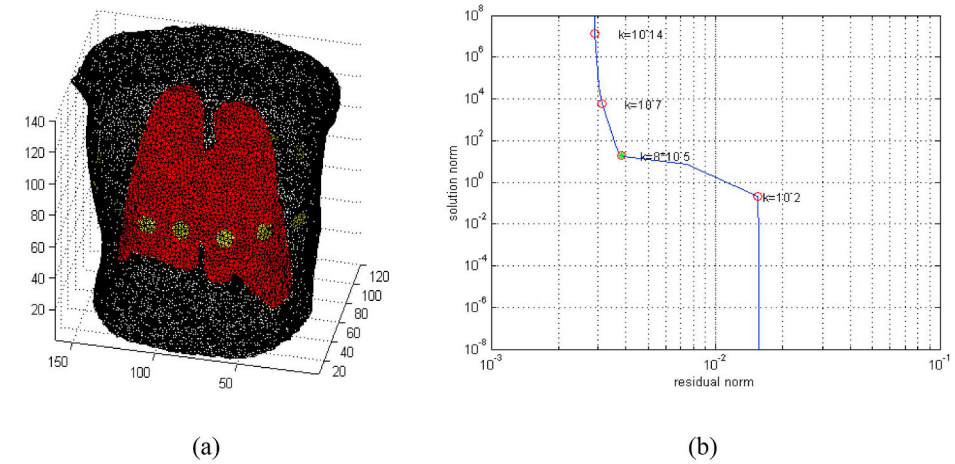

Fig. 9. Image reconstruction using the thorax mesh adapted to the lungs: (a) The mesh used to generate the data, (b) Illustration of the quantitative effect of the global hyperparameter using the L-curve. 3D current density flow simulated between two electrodes based on the thorax mesh of (a): (c) side view, (d) dorsal view. Note, the current streamlines overlaid on the 75th slice of the X-ray CT are also displayed. The vector field was decimated by 10% for improved visualization of the field distribution.

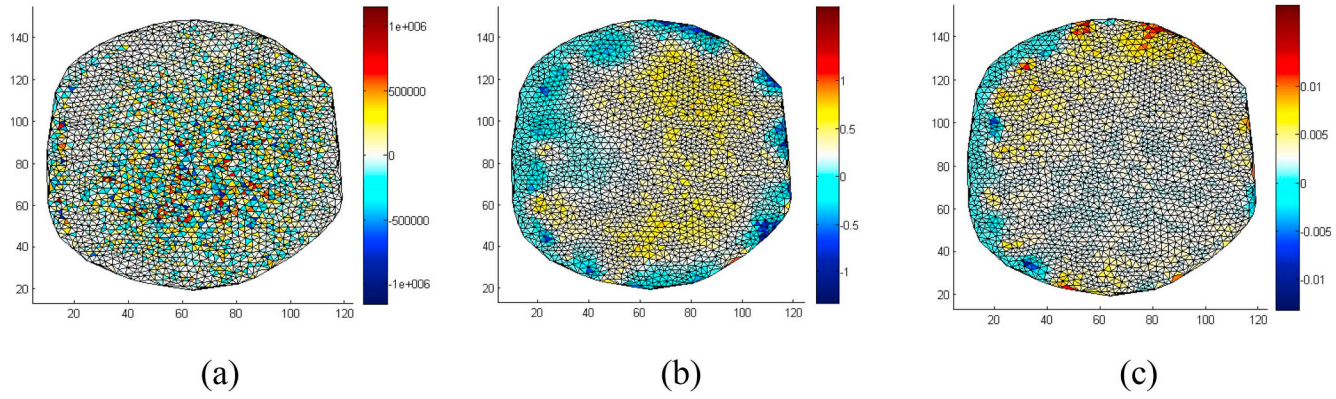

Fig. 10. Evolution of $2^{1/2}D$ reconstructed images with varying hyperparameter values: (a) $\lambda = 10^{-12}$, (b) $\lambda = 10^{-5}$, and (c) $\lambda = 10^{-2}$.

result in greater ill-conditioning of the system matrix.

In the context of EIT, there is a number of 3D real-time imaging studies in the state-of-the-art. In 2016, Schullcke et al. [19], sought the practical feasibility of a double electrode band, using two independent EIT devices for real-time multi-plane imaging. However, the utilized meshes were based on cylindrical phantoms. It would be interesting to explore the use of the models developed in the current research with the approach proposed in Ref. [19] to evaluate performance improvements using realistic models of the thorax and the lungs. A similar study by Wagenaar and Adler [41] explored improvements when using two electrode rings around the thorax for volumetric EIT reconstructions. The goal was to characterize the phantom and the in-vivo performance of 3D EIT with two electrode planes. First, phantom measurements were used to measure the reconstruction characteristics of seven stimulation and measurement configurations. Next, measurements were performed on healthy volunteers as a function of body posture and various electrode configurations. Phantom results indicated that the proposed approach provides reasonable resolution in the electrode plane, however, it is affected by low vertical resolution. Moreover, the study lacked in using adequately realistic meshes so as to augment the quality of the reconstructions, since a cylindrical phantom is an oversimplistic approximation of the human thorax. The approach closest to the present work is that of Grychtol et al. [6], where the capabilities of GREIT were expanded to 3D, by building FEM models from the Visible

Table 2
Mesh statistics for the new forward (FWD) and inverse (INV) meshes.

Aspect ratio histogram	FWD mesh	INV mesh	Histogram (degrees)	Face angle		Dihedral angle	
				FWD mesh	INV mesh	FWD mesh	INV mesh
< 1.5:	646	349	0-10:	3	0	478	15
1.5–2:	6852	3008	10-30:	22861	251	11659	691
2–2.5:	9026	2128	30-50:	53857	10134	23083	3627
2.5–3:	8309	706	50-70:	33398	7849	9899	2638
3-4:	12172	476	70-80:	27220	5294	463	199
4-6:	6043	209	80-110:	46190	5471	26554	4599
6-10:	1742	91	110-130:	3896	112	11407	1443
10-15:	293	4	130-150:	185	3	4799	580
15-25:	36	1	150-160:	2	0	1408	113
25-50:	0	0	160-170:	0	0	488	39
50-100:	0	0	170-175:	0	0	0	0
100-:	0	0	175-180:	0	0	0	0

Human Project data set [42]. However, the lungs in the study were defined based on ellipsoidal geometries in anatomically appropriate regions, thus not fully considering the complex geometry of lung lobes. Moreover, the resulting reconstructions were of low quality and no quantification was provided. In the current study, we introduce realistic and anatomically sound meshes, and show how they can be readily incorporated into existing software to produce 3D EIT reconstructions.

A number of issues need to be considered in order to move towards a 4D model of respiration. Indeed, the Finite Element method is a powerful tool in the simulation of conductivity changes of the lungs.

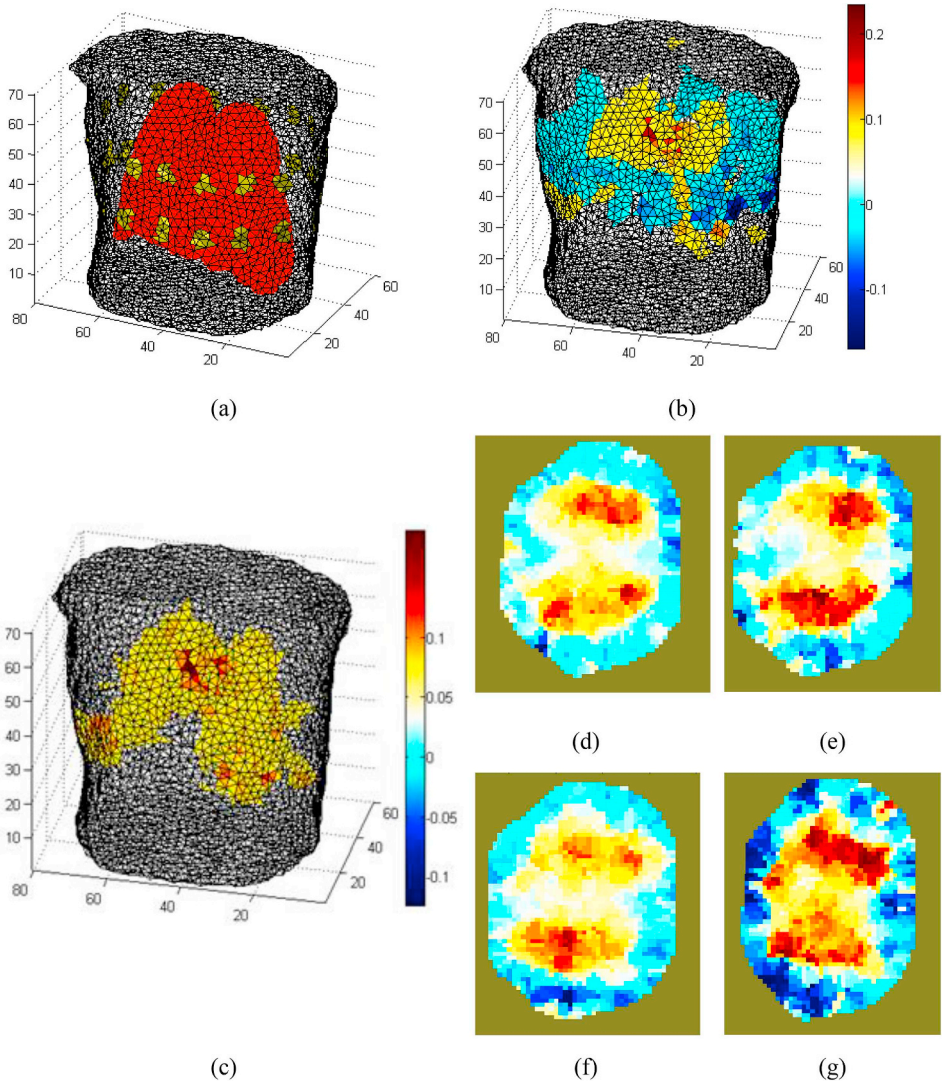

Fig. 11. 3D reconstruction results with inhomogeneity introduced inside the left and right lungs: (a) original mesh with inhomogeneity, (b) reconstructed conductivity, (c) thresholded conductivity, (d) conductivity of (b) at slice Z = 30, (e) conductivity of (b) at slice Z = 35, (f) conductivity of (b) at slice Z = 40.

However, using a time sequence of realistic 3D FEM models of the human organs will result to a significant increase in the number of image artefacts. This is due to the higher ratio of mesh elements, when compared to the number of boundary measurements. Moreover, the convergence speed may be dramatically affected. When 3D models are to be used for both the EIT forward and inverse problems in practice, e.g., at the bedside, the computational domain becomes large and computations need to be carried out over longer time periods. Subsequently, the scale of the problem becomes large and thus, it is essential to use methods, which are as efficient and fast as the available hardware allows. A means forward towards this goal is to investigate large-scale parallel Finite Element computations such as domain decomposition techniques [43], which have been successfully applied in several large-scale flow problems in the mechanical engineering community. The proposed subdivision has two main purposes, namely, (a) to distribute element computations to CPUs in an even manner, and (b) to distribute systems of equations evenly to CPUs for maximum efficiency in the solution process.

In regards to mesh updating, when the requirement is the development of an in-vivo 4D simulation environment, e.g., to visualize in real time the reaction of the lungs as the patient undergoes mechanical ventilation, due to the unstructured nature of the meshes, new mesh updating strategies similar to Ref. [44] are needed to handle the movements of the nodes automatically and reduce the frequency of remeshing. Another interesting technique was proposed in Ref. [45]. This volumetric deformation technique is a Laplacian editing technique, which operates on a tetrahedral mesh rather than the traditional triangular mesh. This offers the advantage of minimizing changes in the volume of tetrahedral elements, thus preventing mesh collapse.

6. Conclusion

We proposed a novel framework for building realistic FEM models of the thorax directly from CT volumes. The generated meshes provide an easy to use platform for fast 3D EIT reconstructions, without oversimplifying organ geometry. They have the potential to pave the way for the incorporation of dynamic models of lung movement during breathing, producing real-time 3D EIT reconstructions, which can be further processed to extract ventilatory parameters. Indeed, the purpose of this contribution is to contribute towards a general purpose framework for the development of 4D FE phantoms for EIT, rather than to rigorously evaluate the performance of existing reconstruction algorithms.

Conflict of interest statement

None Declared.

Acknowledgements

The authors gratefully acknowledge financial support for this research through Grant EP/E029868/1 provided by the Engineering and Physical Sciences Research Council.

References

[1] T. Sunaga, H. Ikehira, S. Furukawa, H. Shinkai, H. Kobayashi, Y. Matsumoto, E. Yoshitome, T. Obata, S. Tanada, H. Murata, Y. Sasaki, Measurement of the electrical properties of human skin and the variation among subjects with certain skin conditions, Phys. Med. Biol. 47 (1) (2001) N11.
[2] C. Gabriel, Dielectric properties of biological tissue: variation with age, Bioelectromagnetics 26 (S7) (2005) S12–S18.
[3] L. Fabrizi, A. McEwan, T. Oh, E.J. Woo, D.S. Holder, A comparison of two EIT systems suitable for imaging impedance changes in epilepsy, Physiol. Meas. 30 (6) (2009) S103–S120.
[4] L. Sophocleous, I. Frerichs, M. Miedema, M. Kallio, T. Papadouri, C. Karaoli, T. Becher, D.G. Tingay, A.H. van Kaam, R. Bayford, A.D. Waldmann, Clinical performance of a novel textile interface for neonatal chest electrical impedance tomography, Physiol. Meas. 39 (4) (2018) 044004(11pp).
[5] T. Murai, Y. Kagawa, Electrical impedance computed tomography based on a finite element model, IEEE Trans. Biomed. Eng. 32 (1985) 177–184.
[6] B. Grychtol, B. Mueller, A. Adler, 3D EIT image reconstruction with GREIT, Physiol. Meas. 37 (6) (2016) 785–800.
[7] S. Aguiar Santos, M. Czaplik, J. Orschulik, N. Hochhausen, S. Leonhardt, Lung pathologies analyzed with multi-frequency electrical impedance tomography: pilot animal study, Respir. Physiol. Neurobiol. 254 (2018) 1–9.
[8] N. Hochhausen, I. Biener, R. Rossaint, A. Follmann, C. Bleilevens, T. Braunschweig, S. Leonhardt, M. Czaplik, Optimizing PEEP by electrical impedance tomography in a porcine animal model of ARDS, Respir. Care 62 (3) (2017) 340–349.
[9] S. Bialka, M. Copik, K. Rybczyk, H. Misiolek, Electrical impedance tomography for diagnosis and monitoring of pulmonary function disorders in the intensive care unit - case report and review of literature, Anaesthesiol. Intensive Ther. 49 (3) (2017) 222–226.
[10] G. Hempel, G. Schulze, H. Wirtz, H. Wrigge, Electrical impedance tomography for confirmation of lung isolation during one-lung ventilation, Anesthesiology 129 (3) (2018) 580.
[11] B.K. Walsh, C.D. Smallwood, Electrical impedance tomography during mechanical ventilation, Respir. Care 61 (10) (2016) 1417–1424.
[12] I. Frerichs, P.A. Dargaville, T. Dudykevych, P.C. Rimensberger, Electrical impedance tomography: a method for monitoring regional lung aeration and tidal volume distribution? Intensive Care Med. 29 (12) (2003) 2312–2316.
[13] G. Franchineau, N. Brechot, G. Lebreton, G. Hekimian, A. Nieszkowska, J.L. Trouillet, P. Leprince, J. Chastre, C.E. Luyt, A. Combes, M. Schmidt, Bedside contribution of electrical impedance tomography to setting positive end-expiratory pressure for extracorporeal membrane oxygenation-treated patients with severe acute respiratory distress syndrome, Am. J. Respir. Crit. Care Med. 196 (4) (2017) 447–457.
[14] B. Vogt, S. Lohr, Z. Zhao, C. Falkenberg, T. Ankermann, N. Weiler, I. Frerichs, Regional lung function testing in children using electrical impedance tomography, Pediatr. Pulmonol. 53 (3) (2018) 293–301.
[15] J. Kobylianskii, A. Murray, D. Brace, E. Goligher, E. Fan, Electrical impedance tomography in adult patients undergoing mechanical ventilation: a systematic review, J. Crit. Care (33) (2016) 35–50.
[16] W.R. Breckon, M.K. Pidcock, Mathematical aspects of impedance imaging, Clin. Phys. Physiol. Meas. 8 (Suppl A) (1987) 77–84.
[17] H.C. Jongschaap, R. Wytch, J.M. Hutchison, V. Kulkarni, Electrical impedance tomography: a review of current literature, Eur. J. Radiol. 18 (3) (1994) 165–174.
[18] A. Adler, J.H. Arnold, R. Bayford, A. Borsic, B. Brown, P. Dixon, T.J. Faes, I. Frerichs, H. Gagnon, Y. Gaerber, B. Grychtol, G. Haehn, W.R. Lionheart, A. Malik, R.P. Patterson, J. Stocks, A. Tizzard, N. Weiler, G.K. Wolf, GREIT: a unified approach to 2D linear EIT reconstruction of lung images, Physiol. Meas. 30 (6) (2009) S35–S55.
[19] B. Schullcke, S. Krueger-Ziolek, B. Gong, U. Mueller-Lisse, K. Moeller, Simultaneous application of two independent EIT devices for real-time multi-plane imaging, Physiol. Meas. 37 (9) (2016) 1541–1555.
[20] B. Schullcke, B. Gong, K. Moeller, Steps towards 3D electrical impedance tomography, IEEE Engineering Medicine Biology Society International Conference, 2015, pp. 5323–5326.
[21] M.G. Crabb, J.L. Davidson, R. Little, P. Wright P, A.R. Morgan, C.A. Miller, J.H. Naish, G.J. Parker, R. Kikinis, H. McCann, W.R. Lionheart, Mutual information as a measure of image quality for 3D dynamic lung imaging with EIT, Physiol. Meas. 35 (5) (2014) 863–879.
[22] B.M. Graham, A. Adler, Electrode placement configurations for 3D EIT, Physiol. Meas. 28 (7) (2007) S29–S44.
[23] D.S. Holder, Electrical impedance tomography (EIT) of brain function, Brain Topogr. 5 (2) (1992) 87–93.
[24] R. Marchand, J.Y. Lu, K. Kabin, R. Rankin, Unstructured meshes and finite elements in space plasma modelling : principles and applications, Advanced Methods for Space Simulations, 2007, pp. 111–143.
[25] B.H. Brown, Electrical impedance tomography (EIT): a review, J. Med. Eng. Technol. 27 (3) (2003) 97–108.
[26] S. Hu, E.A. Hoffman, J.M. Reinhardt, Automatic lung segmentation for accurate quantitation of volumetric X-ray CT images, IEEE Trans. Med. Imaging 20 (6) (2001) 490–498.
[27] J. Vandemeulebroucke, D. Sarrut, P. Clarysse, The POPI model, a point-validated pixel-based breathing thorax model, International Conference on the Use of Computers in Radiation Therapy, 2007.
[28] F. Yang, R.P. Patterson, The contribution of the lungs to thoracic impedance measurements: a simulation study based on a high resolution finite difference model, Physiol. Meas. 28 (7) (2007) S153–S161.
[29] E. Puppo, D. Panozzo, R.G.B. Subdivision, IEEE Trans. Vis. Comput. Graph. 15 (2) (2009) 295–310.
[30] C. Loop, Smooth Subdivision Surfaces Based on Triangles, Master Thesis, Dept. of Mathematics, Univ. of Utah, 1987.
[31] H. Si, TetGen: A Quality Tetrahedral Mesh Generator and Three-Dimensional Delaunay Triangulator, (2006) http://tetgen.berlios.de.
[32] J. Behari, S.K. Guha, P.N. Agarwal, Temperature dependence of the electrical conductivity of bone, Connect. Tissue Res. 2 (4) (1974) 325–328.
[33] A. Adler, W.R. Lionheart, Uses and abuses of EIDORS: an extensible software base for EIT, Physiol. Meas. 27 (5) (2006) S25–S42.
[34] A. Adler, W.R. Lionheart, EIDORS: towards a community-based extensible software base for EIT, Electrical Impedance Tomography Conference, 2005.
[35] B.S. Kim, A.K. Khambampati, S. Kim, K.Y. Kim, Image reconstruction with an adaptive threshold technique in electrical resistance tomography, Meas. Sci.

Technol. 22 (10) (2011) 1–12.
[36] F.B. Hildebrand, Introduction to Numerical Analysis, Dover Publications, 1987.
[37] H. Edelsbrunner, Geometry and Topology for Mesh Generation, Cambridge University Press, 2001.
[38] P. Kantartzis, M. Abdi, P. Liatsis, Stimulation and measurement patterns versus prior information for fast 3D EIT: a breast screening case study, Signal Process. 93 (10) (2013) 2838–2850.
[39] M. Bern, D. Eppstein, Mesh generation and optimal triangulation, Computing in Euclidean Geometry, vol 4, 1995, pp. 47–123.
[40] V.N. Parthasarathy, C.M. Graichen, A.F. Hathaway, A comparison of tetrahedron quality measures, Finite Elem. Anal. Des. 15 (3) (1994) 255–261.
[41] J. Wagenaar, A. Adler, Electrical impedance tomography in 3D using two electrode planes: characterization and evaluation, Physiol. Meas. 37 (6) (2016) 922–937.
[42] M.J. Ackerman, The Visible Human Project: a resource for anatomical visualization, Stud. Health Technol. Inf. 52 (Pt 2) (1998) 1030–1032.
[43] D. Rixen, F. Magoulès, Domain decomposition methods: recent advances and new challenges in engineering - Preface, Comput. Methods Appl. Mech. Eng. 196 (8) (2007) 1345–1346.
[44] A.A. Johnson, T.E. Tezduyar, Mesh update strategies in parallel finite element computations of flow problems with moving boundaries and interfaces, Comput, Methods Appl. Mech. Eng. 119 (1–2) (1994) 73–94.
[45] S. Basting, A. Quaini, S. Čanić, R. Glowinski, Extended ALE Method for fluid–structure interaction problems with large structural displacements, J. Comput. Phys. 331 (2017) 312–336.